Growth of Spheroidal Graphite on Nitride Nuclei: Disregistry and Crystallinity During Early Growth

D.M. STEFANESCU, A. CRISAN, G. ALONSO, P. LARRAÑAGA, and R. SUAREZ

The graphite phase resulting from the stable solidification of iron-carbon-silicon alloys can have a variety of morphologies, from lamellar to spheroidal, including undesired degenerated morphologies. Spheroidal graphite is preferred when high strength and ductility are required. Understanding the nucleation and growth mechanism of graphite will improve control of its morphology during industrial processing. The crystalline structure of spheroidal graphite in iron-carbon-silicon alloys exhibits a multi-regions substructure. Literature opinions on the degree of crystallinity of the core of the spheroid are divergent. Unconvincing explanations are offered. The ability of nitrides to serve as graphite nuclei is questioned because of the high linear disregistry. To bring some clarity into the early crystallization of graphite in iron melts, interrupted solidification samples were examined through scanning electron microscopy. Disregistry calculations and thermodynamic analysis demonstrated that certain nitrides are favorable for graphite nucleation. Some unique pictures showing graphite platelets growing out of the nucleus were obtained from deep-etched samples. They bring evidence of the disorientation of graphite platelets growing around the graphite nuclei for the particular case of Mg-Al-Si nitrides. It is suggested that the low crystallinity observed in the core of some graphite spheroids is the result of this random orientation of the graphite platelets growing on nucleating inclusions during early solidification and of subsequent curved-circumferential growth.

I. BACKGROUND

IN recent years, significant work was devoted to the understanding of the nucleation, crystalline structure and growth mechanisms of graphite in iron-carbon-silicon alloys. The crystalline structure of spheroidal graphite (SG) includes up to four distinctive regions.[1–4] The regions result from changes in the growth kinetics of the graphite as it transits through four distinct stages: stage I—growth of graphite in direct contact with the liquid; stage II—growth of graphite during the eutectic reaction through carbon diffusion from the melt through the austenite shell; stage III—growth in the solid state between the eutectic and eutectoid temperature, because of decreased carbon solubility in austenite; stage IV—growth in the solid state between the eutectoid and room temperature, because of decreased carbon solubility in ferrite. Usually, the growth in stage IV cannot be distinguished from that in stage III. Two regions are typical if the sample is obtained through interrupted solidification or rapid cooling, and three regions may be visible on room temperature samples. In Figure 1(a), graphite platelets, growing concentric to the (MgCa)S nucleus, are seen. This core region is formed during early solidification, when graphite growth occurs in direct contact with the liquid. The growth mechanism in this stage is, most of the time, curved-circumferential crystal or foliated growth.[3,5,6] The graphite platelets in the core are rather disorganized (Figures 1(a) and 2(a)). For reasons yet to be explained, a growth kinetics transition produces stacking of the graphite platelets into clusters of polyhedral blocks and highly curved graphite aggregates resulting in conical (pyramidal) sectors made of platelets parallel to one another. While for well-shaped spheroidal graphite this is believed to be the product of divorced eutectic solidification during stage II,[3,6] a recent synchrotron radiation X-ray study by Yamane et al. [7] found that early solidification of imperfect SG from the liquid can also proceed with columnar conical sectors. This is also consistent with degenerated graphite found in flotation zones in large

D.M. STEFANESCU is with the The Ohio State University, Columbus, OH, and also with the The University of Alabama, Tuscaloosa, AL. Contact e-mail: stefanescu.1@osu.edu A. CRISAN is with the Transilvania University of Brasov, Brasov Romania. G. ALONSO and P. LARRAÑAGA are with IK4-Azterlan, Durango, Bizkaia, Spain. R. SUAREZ is with IK4-Azterlan, Durango, and also with the Veigalan Estudio 2010, Durango, Bizkaia, Spain.
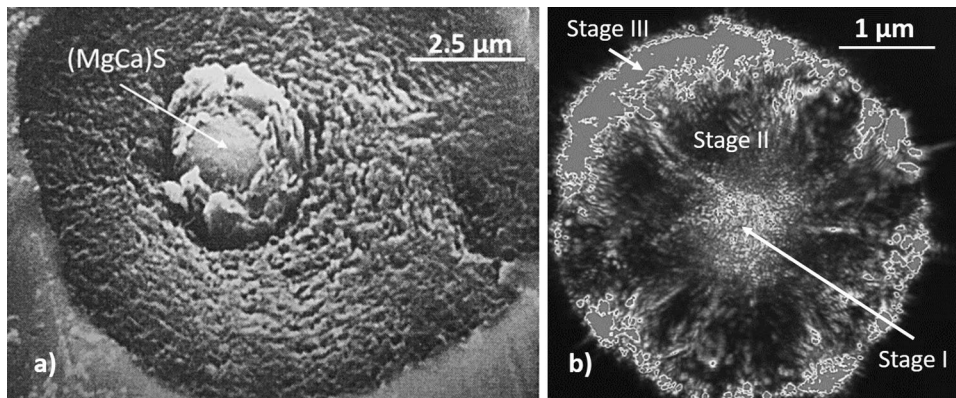
Fig. 1—Graphite spheroids exhibiting regions with different crystallography: (*a*) plasma-etched image of graphite spheroid obtained through interrupted solidification from the liquid (1288 °C), from Ref. [1] with permission; (*b*) confocal scanning laser image of a graphite spheroid after cooling to room temperature, from Ref. [2] with permission.
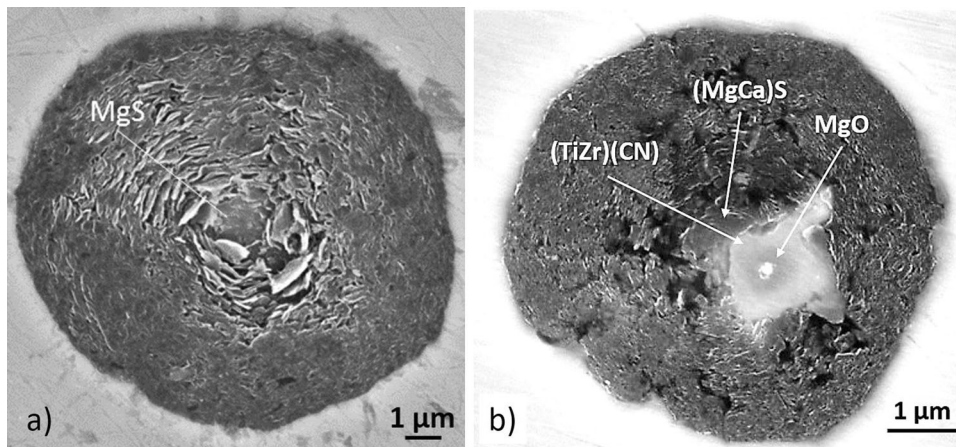

Fig. 2—SEM images showing nucleation of graphite platelets: (*a*) on a MgS inclusion in a magnesium-modified iron (3.3C, 2Si, 0.009S, 0.014Ti, 0.044Mg; all in mass percent), from Ref. [3] with permission; (*b*) on (TiZr)(CN) and (MgCa)S inclusions in a magnesium-modified iron (3.78C, 1.93Si, 0.009S, 0.03Ti, 0.038Mg; all in mass percent), from Ref. [17] with permission.

castings, *e.g.*, chunky graphite,[8] and with growth in the initial stages in compacted graphite iron (tadpole graphite),[6] where polyhedral blocks were found growing out of an initial spherical graphite. The main possible mechanisms of polyhedral blocks/conical sectors are layer growth, foliated crystal stacking, and helical growth (negative wedge disclination, not to be confused with the cone-helix mechanism of Double and Hellawell).[6] Three regions are seen in Figure 1(b). The third region results from growth in stage III and IV.

TEM work by several investigators concluded that while the graphite generated in stage II is highly crystalline, the core region has low crystallinity or is amorphous. In samples prepared by the focused ion beam (FIB) method, Hara *et al.*[9] found that the central region of a graphite spheroid in ductile iron is "a mixture of distorted and ordered graphite regions as well as some amorphous carbon, graphene and fullerenes." They argued that these lower density regions are most likely growth faults, caused by a period of imperfect radial graphitic growth. An amorphous carbon region was also identified in the center of graphite

spheroids in quenched and annealed carbon steel by He *et al.*[10] They posited that the nucleation sites are probably dissolving cementite particles in the martensite. Examining graphite in the as-cast thin-wall castings with mixed stable/metastable solidification, Laffont *et al.*[11] found a two-stage structure characterized by an inner zone where graphite is "disoriented" but not amorphous, and an outer zone where it is well crystallized. However, in samples fully graphitized following holding at temperatures in the austenite field, the graphite spheroids exhibited well-crystallized sectors radiating from the nucleus. Other TEM work where the samples were prepared by FIB did not report any randomly oriented graphite platelets.[4,12,13] The highly ordered core of spheroids found in such research may be the result of recrystallization during cooling. Certainly, recrystallization is active during annealing [11] producing fully crystalline structures.

Explanations of the low-crystallinity or amorphous structure of the core of the graphite spheroid are few and unconvincing, revolving around the stress on the graphite.[11,14] Yet, there is experimental evidence that the crystallography of the nuclei and the aggregation of the

various inclusions forming the nucleus affects graphite growth. Indeed, He et al.[10] and then Li et al.[15] found that, in heat-treated carbon steel, graphite may nucleate on AlN inclusions which are about half the diameter of the 18-μm-diameter SG. The large AlN can provide multiple nucleation sites on the different facets of the nitride. Thus, in graphite with AlN nuclei, the graphene layers grow on the AlN nuclei at different angles (35, 40, and 90 deg) and not necessarily parallel to the graphite/AlN interface. This implies that the substrate on which the graphene grows (the nucleus) directly affects the morphology of the aggregate. A similar conclusion was reached by Alonso et al.[3,16] who demonstrated that complex inclusions, resulting from the use of inoculants in the melt processing of ductile iron, nucleate graphite that is often less than spheroidal. A nucleus consisting of spherical MgS (Figure 2(a)) is surrounded by better organized graphite platelets than a complex nucleus including a carbonitride (Figure 2(b)[17]).

Nitrides and/or carbonitrides with cubic morphology have been assumed or detected as nuclei for lamellar,[18] compacted,[19] and spheroidal graphite.[10,15,20–22] Yet, their ability to nucleate graphite was questioned because of their high linear disregistry with the hexagonal structure of the graphite.

Igarashi and Okada[21] investigated graphite spheroids in Mg-treated iron using SEM with EDS, EPMA, AES, and TEM. They found that SG nucleated on ~ 1-μm-diameter spherical (MgCa)S inclusions, with occasional (MgSiAl)N nitrides attached. MgO spherical inclusions of ~ 0.2 μm diameter were detected in or at the surface of (MgCa)S. Nakae and Igarashi[23] found that for base irons with less than 0.005 pct S spheroidal graphite nucleates on spherical MgS following Mg treatment, but the nuclei are (MgSiAl) nitrides when the S content is less than 0.022 pct. The shape of these nitrides appears to be cuboidal with a size of 0.5 to 1 μm. Alonso et al.[17] found that the determining factor in the selection of the type of nitride for nucleation is the Ti content. Indeed, in irons with 0.009 pct S, Mg-Si-Al nitrides were found in the nuclei in the low-Ti (0.014 pct) iron, while the nuclei contained Ti(CN) carbonitrides in the higher-Ti (0.03 pct) iron.

Even though, as discussed earlier, the role of nucleating inclusions on the growth morphology of SG appears to be significant, limited effort has been made to investigate graphite growth in the immediate vicinity of the nucleus. The goal of this work is twofold: (i) to confirm the viability of nitrides as nucleants for spheroidal graphite through SEM in-depth analysis and through calculation of disregistry, and (ii) to bring some clarity into the early crystallization of graphite in iron melts, which may explain the lower crystallinity of the core of some spheroidal graphite.

II. EXPERIMENTAL STRATEGY

A. Melting and Sample Preparation

The experimental melts were produced in a 100 kg medium frequency induction furnace from charging materials that included 43 pct ductile iron returns and 57 pct high-purity pig iron. Carbon and silicon composition corrections were made after melting as needed through additions of graphite (99 pct C) and ferro-silicon (74.6 pct Si, 0.3 pct Ca, 0.7 pct Al, balance Fe). Ferro-titanium (68.8 pct Ti, 3.6 pct Al, balance Fe) was added in one melt.

After superheating to 1500 °C, the iron was transferred into the pouring ladle. The Mg treatment consisted in addition of 1.1 mass pct of the melt weight of Fe-Si-Mg alloy (47.2 pct Si, 6.02 pct Mg, 0.88 pct Lanthanides, 0.3 pct Mn, 1.15 pct Ca, 0.24 pct Al) on the bottom of the pouring ladle before filling it (sandwich method). No post-inoculation was done. From each melt, standard thermal analysis cups (36 × 36 × 43 mm) were poured. Solidification of the cups was interrupted by quenching in brine (to increase the thermal conductivity) immediately after filling the cup, or after 60 seconds, to provide information on the microstructure at various stages during solidification. After cooling to room temperature, the cups were sectioned and prepared for metallographic examination. The interrupted solidification experimental technique was used to produce graphite spheroids that have grown predominantly in the liquid in Mg-modified irons, such that their morphology is not affected by diffusional growth through the austenite shell and/or by crystallization of amorphous carbon.

The chemical composition of all samples is given in Table I. Note the two levels of Ti. The selection of particular Ti contents was based on our previous observations[17,24] that a low level of Ti is conducive to nucleation on (MgAlSi)N nitrides, while a higher Ti produces nuclei that include Ti(CN) carbonitrides.

B. Characterization

The material for the SEM analysis of graphite morphology was obtained from the interrupted solidification thermal analysis cups. After cooling to room temperature, the cups were sectioned and polished. Some samples were deep-etched (ambient temperature 40 seconds etching with a 40 pct nitric acid in water solution, followed by cleaning for five seconds in 50 pct hydrochloric acid in water solution) to remove the matrix surrounding the graphite.

The deep-etched and unetched samples were then examined with a Field Emission Gun Scanning Electron Microscope (FEG-SEM). An Ultra PLUS Carl Zeiss SMT with 0.8-nm resolution at 30 kV in the Scanning Transmission Electron Microscopy (STEM) mode, in combination with an X-Max 20 Oxford Instruments Energy-Dispersive X-ray Spectroscopy (EDX) detector

Table I. Chemical Composition (Mass Percent) of Experimental Cast Irons

Melt	C	Si	Mn	P	S	Mg	Ti
1	3.57	2.03	0.15	0.012	0.005	0.014	0.008
2	3.64	1.97	0.16	0.012	0.005	0.014	0.037

was used to determine the local chemistry of inclusions in the graphite nuclei. Three detectors were used for the generation of images: (a) in-Lens detector (annular SE detector) for the surface structure; (b) Everhart-Thornley type detector (SE2) for topography; (c) Angular Selective Backscattered electron detector (AsB) for compositional contrast. In addition, spectrums, mappings, and line scans were also generated. An example of this analysis is given in Figures 5, 6, and 7, and will be discussed later in this paper.

III. RESULTS AND DISCUSSION

A. SEM Analysis

A series of three SEM micrographs of an imperfect graphite spheroid from the low-Ti iron (0.008 pct Melt 1) is presented in Figure 3. The graphite is encapsulated in an austenite shell, which is surrounded by ledeburite formed during quenching (Figure 3(a)). Two regions are seen on the graphite aggregate: a core corresponding to growth in contact with the liquid, surrounded by an austenite layer formed during quenching of the low-carbon region surrounding the graphite spheroid. Higher magnifications in Figures 3(b) and (c) reveal graphite platelets with highly disorganized orientation growing out of the nucleus and in its immediate vicinity. The nucleus for the graphite is an Mg-Al-Si nitride, as proved by the EDX spectrum in Figure 4. These nitrides that have a hexagonal lattice were consistently found to serve as nuclei in low-sulfur (< 0.009 pct) low-titanium (< 0.014 pct) irons modified with magnesium.[17]

Nucleation of graphite spheroids on Mg-Al-Si nitrides was first observed by Igarashi and Okada.[20] Diffraction and compositional analyses of Solberg and Onsøien[22] concluded that the Mg-Al-Si nitrides have a trigonal superstructure space group $P6_3mc$ belonging to the hexagonal family derived from a hexagonal AlN-type fundamental cell. Based on the compositional analysis, the particles were suggested to have the chemical formula $AlMg_{2.5}Si_{2.5}N_6$. The same authors also stated that there is no obvious crystallographic similarity between the nitride particle and the graphite. This statement generates the need for further argumentation of the capability of these nitrides to serve as nuclei for spheroidal graphite.

Higher titanium content of 0.037 pct (Melt 2) generated the conditions for the formation of complex inclusions acting as nucleants for SG. An example is provided in Figure 5, which shows a nucleus composed of a spherical Mg-Ca sulfide on which a cubic Ti carbonitride has nucleated, followed by nucleation of spheroidal graphite. Confirmation of the composition of these inclusions is provided by EDX/SEM spectrums on the same figure, and by the X-ray composition maps in Figure 6 and the X-ray concentration graphs in Figure 7. Just as for the Mg-Al-Si nitride, the high linear disregistry of the Ti(CN)[19] does not support the possibility that these compounds are good nucleants for graphite. Yet, experimental evidence demonstrates that they do nucleate graphite. The following discussion will include thermodynamics and crystallographic arguments.

B. Thermodynamic Considerations

From compilations of the standard free energy of formation of simple nitrides that may be relevant to graphite nucleation in References 17 and 25, we summarize -580 kJ/mol for TiN, -538 kJ/mol for AlN, -118 kJ/mol for Mg_3N_2, and -163 kJ/mol for TiC. The Ti and Al nitrides have relatively low energies of formation, higher than MgO (-858), but lower than MgS (-294), both proven as common nuclei for SG. These last two values are somehow different than the energies at 1600 K quoted by Igarashi and Okada[21] that are -232 kJ/mol and -401 kJ/mol for MgS and MgO, respectively. It appears that some combinations of Mg_3N_2 with AlN, and of TiC with TiN, are occurring, as nucleation was documented on Mg-Al-Si nitrides and Ti(CN) but was only seldom, if at all, reported on Mg_3N_2 or TiC.

The $AlMg_{2.5}Si_{2.5}N_6$ compound identified by Solberg and Onsøien[22] can be written as the stoichiometric compound $(AlN)_6(Mg_3N_2)_5(Si_3N_4)_5$ in which the aluminum nitride is the dominant compound. However, it is also possible that the complex nitride is associative,
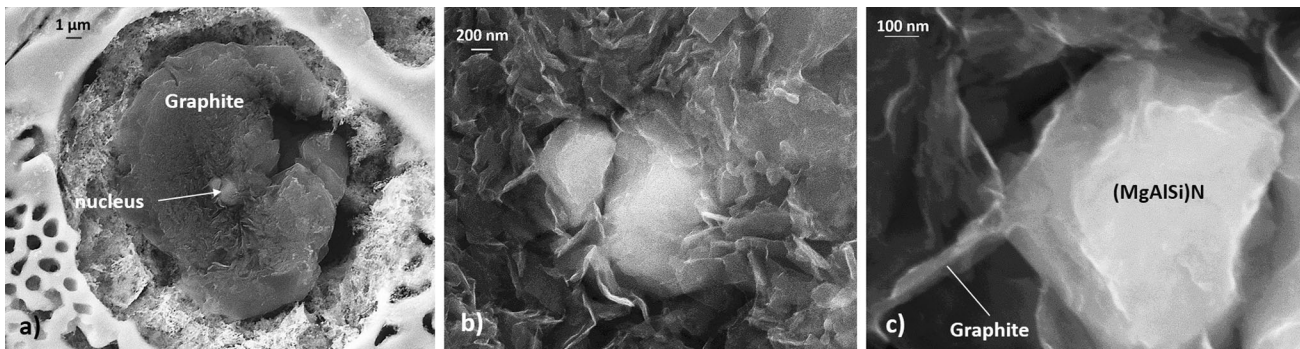

Fig. 3—SEM images from a deep-etched sample obtained from a magnesium-modified iron (Melt 1): (*a*) spheroidal graphite growing on a nucleus; (*b*) higher magnification of (*a*) showing the nucleus made of two Mg-Al-Si nitrides; (*c*) higher magnification of (*b*) showing graphite platelets nucleating on the Mg-Al-Si nitride.
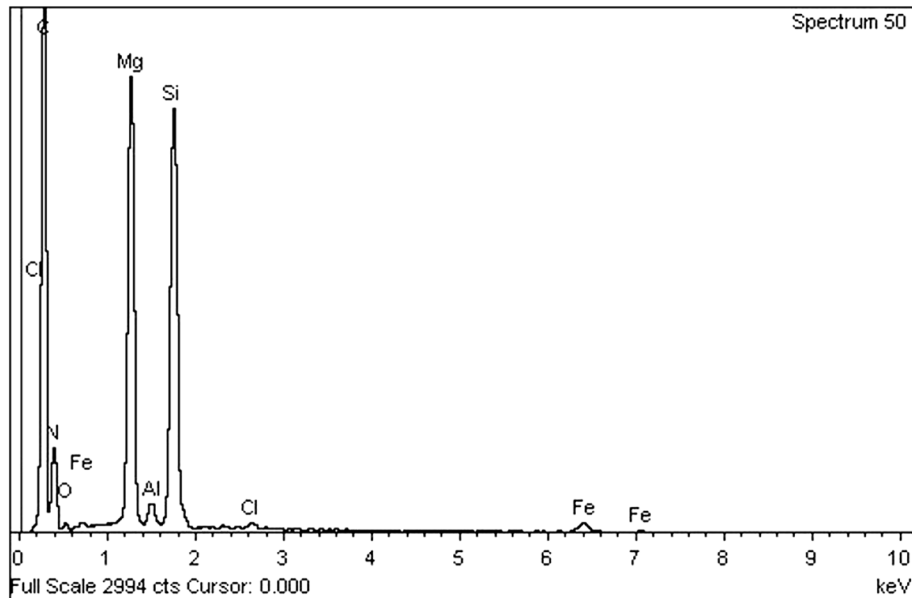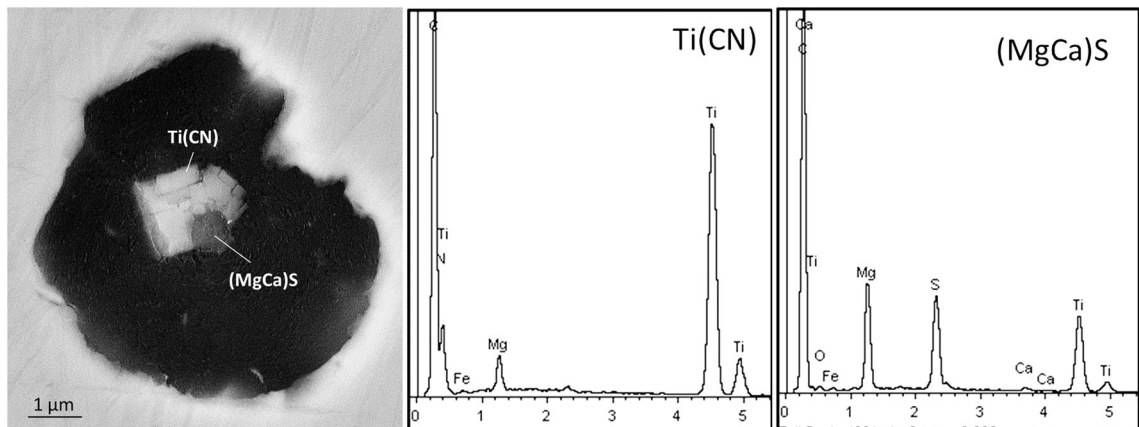
Fig. 4—EDX analysis of the nitride in Fig. 3.

Fig. 5—SEM image of graphite nucleating on an (MgCa)S and Ti(CN) nucleus and corresponding EDX/SEM spectrums.

resulting from the successive growth of the three nitrides. It has been documented that in low-sulfur, low-titanium magnesium-modified melts, magnesium sulfides (or complex magnesium sulfides), nucleating many times on magnesium oxides, are frequent nuclei (Figure 2(a)). As the energy of formation of aluminum and titanium nitrides is positioned between that of MgO and MgS, it is sufficiently low for nucleation of graphite. The complex Mg-Al-Si nitride in Figure 3 appears to also be thermodynamically capable to act as a substrate, in particular if the compound is associative, with Mg_3N_2 nucleating on AlN. This is also true for the Ti(CN) nucleated on Mg(CaS) in Figures 2(b) and 5.

C. Disregistry Calculations

Heterogeneous nucleation of graphite requires the formation of bonds between the carbon atoms and atoms on the surface of the nucleant (Mg, N, Al, S, *etc.*)

so that the carbon atoms migrate from the liquid to stable positions. If these positions match positions belonging to planes in the graphite crystal, graphite grows occurs. Thus, to bring further support of the nucleation ability of Mg-Si-Al nitrides, planar disregistry calculations between the crystalline structure of graphite and the nitrides were performed, to find planes and cells within the graphite crystal having a close match with those on the surfaces of the nucleant crystal.

Planar disregistry rather than the Turnbull/Vonnegut linear disregistry was used, because, according to Bramfitt,[26] the Turnbull/Vonnegut equation cannot be applied to crystallographic combinations of two phases with planes of differing atomic arrangements (in this case cubic nitride and hexagonal graphite). For linear disregistry, a value of 10 pct (lattice misfit) was found to be the higher limit for heterogeneous nucleation on metal powders deposited on the surface of Zn, A1, Mg, Sn, Pb, Cu, and Sb castings.[27] A planar disregistry of
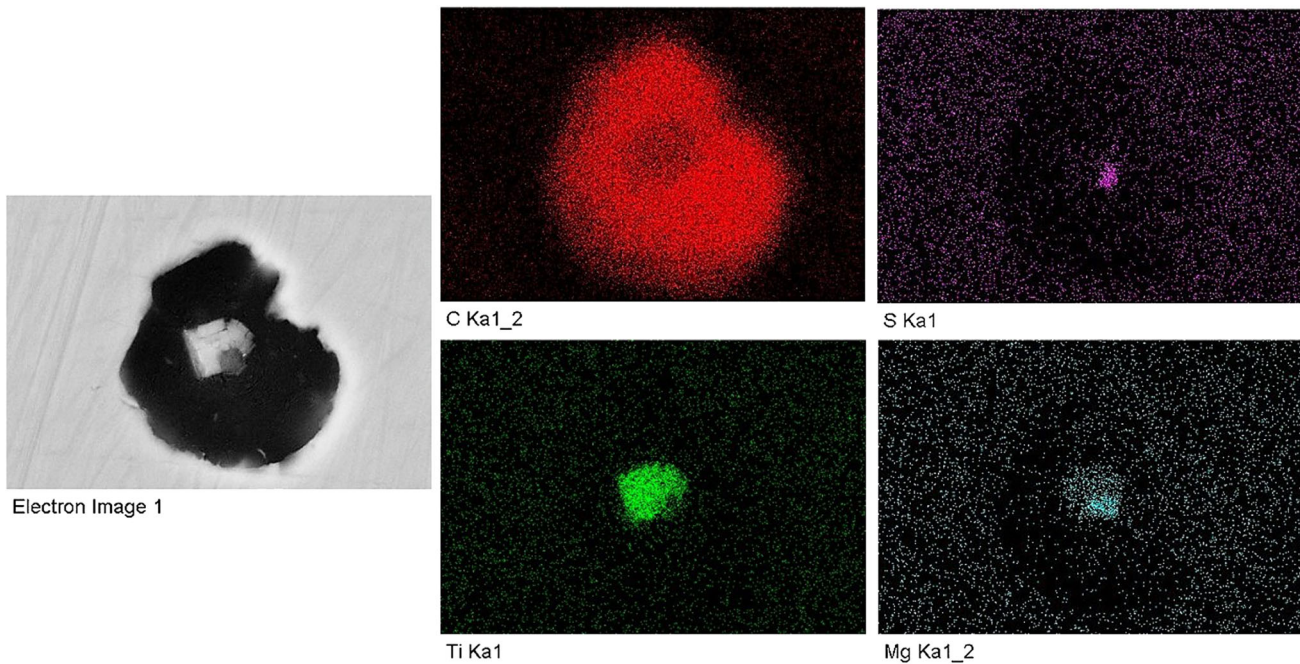
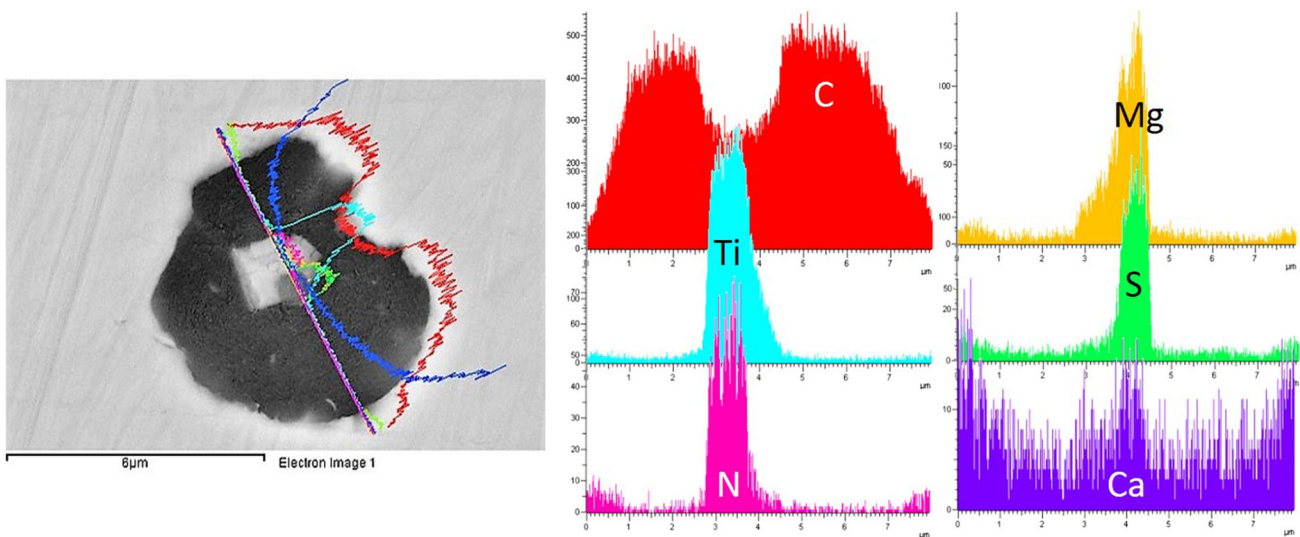Fig. 6—X-ray composition maps for the nucleus in Fig. 5.

Fig. 7—X-ray concentration line scan graphs for the nucleus in Fig.5.

5.9 pct was considered to be indicative of a highly effective nucleant and one of 11.2 pct moderately effective in the evaluation of nucleants for pure iron by Bramfitt. Values smaller than 7.5 pct were found favorable for nucleation of spheroidal graphite on silicates by Skaland.[25] While disregistry calculation of the complex (MgAlSi)N is not possible because of the absence of necessary data on its crystallographic structure, calculation will be performed for the magnesium and aluminum nitrides.

The calculation of planar disregistry was performed with crystal parameter at the standard temperature of formation of the particular crystal. Calculations were

based on the specifics of the graphite lattice shown in Figure 8. Mg_3N_2 has a cubic crystalline structure, space group $Ia\overline{3}$, with the lattice parameter $a = 0.995$ nm.[28] In this cubic structure, the metal atoms are in general positions, 48e of $Ia\overline{3}$ (x, y, z, $etc.$) and there are two kinds of N atom: N(1) in position 8b (1/4, 1/4, 1/4, $etc.$) and N(2) in positions 24d (x, 0, 1/4, $etc.$).[29] The atoms N(2) belonging to the (010) plane on the directions [001] and [100] form square lattices on the face of the crystal, with the side equal to the lattice parameter. A particular aspect is the fact that the ratio between the lattice parameter of Mg_3N_2 and the lattice parameter of the basal plane of the graphite is an almost integer number

(9.95/1.42 = 7.007). For this reason, planes that contain C atoms positioned in squares with sides close to 0.995 nm were sought after in the graphite lattice. Four such planes (P_o, P_1, P_2, P_3) that belong to the families annotated with the Miller indices and run through the origin of the coordination system are presented in Figure 8. They contain graphite atoms positioned in the basal graphene planes, or between basal planes positioned at one, two, or three parametric distances in the c-direction. In each of these planes, cells containing carbon atoms in the corners with interatomic distances close to that in the unit cell of Mg_3N_2 were identified. In these cells, the coordinates of the carbon atoms (directions and interatomic distances) were calculated. For each cell, the origin of the coordination axis was considered as follows: in position A in Figure 8 for planes P_o and P_2; in position B in Figure 8 for planes P_1 and P_3; in position C in Figure 8 for plane P_4. They are summarized in Table II, and a graphic example is shown in Figure 9.

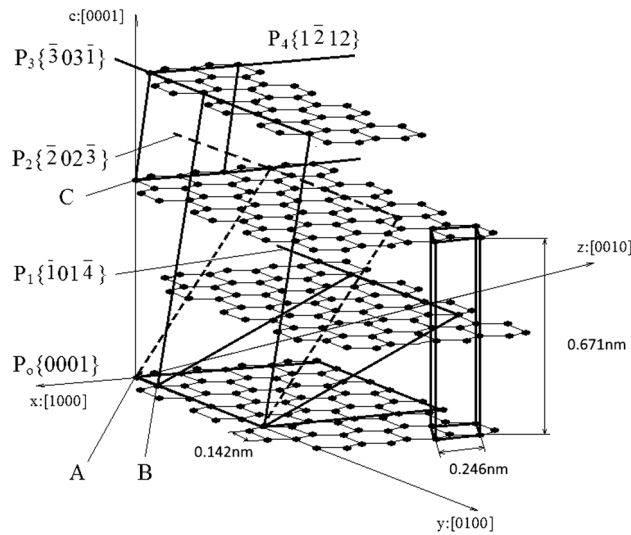The planar disregistry was calculated with the following equation,[26] which includes angular differences between the crystallographic directions within the planes:

$$\delta = \sum_{i=1}^{3} \frac{1}{3} \left[\frac{\left| d_{[uvw]}^{Mg_3N_2} \cos\alpha - d_{[uvw]}^{G} \right|}{d_{[uvw]}^{Mg_3N_2}} \right] \cdot 100, \qquad [1]$$

where $[uvw]_{Mg_3N_2}$ is a low-index direction in $(hkl)_{Mg3N2}$, $[uvw]_G$ is a low-index direction in $(hkl)_G$, $d_{[uvw]}^{Mg_3N_2}$ is the interatomic spacing along $[uvw]_{Mg_3N_2}$, $d_{[uvw]}^{G}$ is the interatomic spacing along $[uvw]_G$, and α is the angle between the $[uvw]_{Mg_3N_2}$ and the $[uvw]_G$. The results of planar disregistry (δ) calculations are presented in Table II.

The small values of these planar disregistries, and in particular δ_0 and δ_2, suggest near perfect coherency and hence the possibility of graphite nucleation on Mg_3N_2. The most favorable are the plane P_0 and P_2, in which cells with dimensions almost identical with the unit cell of Mg_3N_2. were found. In the first case, it may be assumed that the graphene layers grow initially on the corners of the magnesium nitride cells, and then continue to grow perpendicular to the surface of the cells (c-growth direction of spheroidal graphite). In the second case, graphite growth occurs with a dihedral angle orientation of 42°16′39″ with respect to the face of the nitride, as described in the Lux model.[30] Favorable planes were also found for the P_1 and P_3 family of planes. A total of 18 families of planes include cells favorable to graphite growth.

It was interesting to also explore the Mg_3N_2/graphite linear disregistry. In the Mg_3N_2 lattice, the interatomic distances are close to the C distances in the graphite lattice. Such distances and the linear disregistry calculated with Eq. [2] are given in Table III.

$$\delta_l = \left(\frac{\left| \left(d_{[uvw]}^{Mg_3N_2} - d_{[uvw]}^{G} \right) \right|}{d_{[uvw]}^{Mg_3N_2}} \right) \cdot 100, \qquad [2]$$

where notations are similar to those in Eq. [1]. The 4.41 pct linear disregistry between the Mg-Mg and the C-C atoms is also in the range favorable for nucleation

Fig. 8—Spatial geometry of the crystallographic lattice of graphite.

Table II. Data for Calculation of Planar Disregistry Graphite Mg_3N_2

No.	Planar Disregistry Between	$[uvw]_{Mg_3N_2}$	$[uvw]_G$	$d_{[uvw]}^{Mg_3N_2}$	$d_{[uvw]}^{G}$	α (Deg)	$d_{[uvw]}^{Mg_3N_2} \cdot \cos\alpha$	δ (Percent)
1	P_0 and Mg_3N_2	[100]	[0100]	0.995	0.994	0	0.995	
2		[101]	[$\bar{4}$740]	1.407	1.399	17′23″	1.4068	$\delta_0 = 0.59$
3		[001]	[$\bar{4}$040]	0.995	0.984	0	0.995	
4	P_1 and Mg_3N_2	[100]	[0100]	0.995	0.852	0	0.995	
5		[101]	[$\bar{4}$641]	1.407	1.344	5°40′29″	1.337	$\delta_1 = 6.47$
6		[001]	[$\bar{4}$041]	0.995	0.1040	0	0.995	
7	P_2 and Mg_3N_2	[100]	[0100]	0.995	0.994	0	0.995	
8		[101]	[$\bar{3}$732]	1.407	1.408	5′52″	1.407	$\delta_2 = 0.125$
9		[001]	[$\bar{3}$032]	0.995	0.997	0	0.995	
10	P_3 and Mg_3N_2	[100]	[0100]	0.995	0.852	0	0.995	
11		[101]	[$\bar{1}$613]	1.407	1.341	5°34′11″	1.400	$\delta_3 = 7.57$
12		[001]	[$\bar{1}$013]	0.995	0.1036	0	0.995	

of graphite. The small linear disregistry between the N-N and C-C atoms, in the range of 0 to 10.06 pct, also supports the possibility of graphite nucleation on Mg_3N_2.

A similar analysis was conducted for AlN, which has a hexagonal lattice ($P6_3mc$—space group) with the parameters a = 0.311 nm and b = 0.498 nm.[22,31] In the family of planes $\{10\bar{1}0\}$, $\{01\bar{1}0\}$, $\{1\bar{1}00\}$ and their symmetrical planes with respect to the [0001] axis, the Al and N atoms are positioned such as to form rectangles with atoms Al-Al or N-N in the corners, with the sides equal to the parameters of the crystalline lattice. In the graphite lattice in Figure 8, the family of planes $\{1\bar{2}12\}$, including plane P_4:($1\bar{2}12$), was identified as containing an elementary cell compatible with the prism faces of the hexagonal AlN crystal. Calculations were performed for the disregistry between a lateral face of the AlN crystal and the cell in plane P_4:($1\bar{2}12$) in Figure 8. The same reference system as that for graphite was used for spatial orientation of the AlN crystal. A lateral face contained

in the $\{10\bar{1}0\}$ family of planes and parallel to the y0z plane was selected. The data used for calculation are presented in Table IV.

Using Eq. [1]. and the data in Table IV, a disregistry δ_4 = 7.586 pct was calculated. This implies that graphite can grow on the prism faces of AlN, with the basal planes oriented at an angle of 53°49′46, as described in Lux model.[31] Six such families having the disregistry δ_4 were found. We further note that the disregistry values calculate for Mg_3N_2 and AlN range from 0.59 to 7.586 pct.

As a general comment, we note that a study through process modeling by quantic methods (density functional theory) could produce important information of the bond energy between the C atoms and atoms of the nucleant for the specific thermodynamic conditions in cast iron. This may allow calculation of the size of the nucleus, and eventually a better understanding of the associate phenomena conducive to improved process control in practice.

Having demonstrated that the thermodynamic data and disregistry calculations for Mg_3N_2 and AlN support the assertion that both nitrides are possible nucleants for graphite, we will now turn our attention to the issue of the disorganized or low crystalline structure of the graphite around the nucleus found by some researchers.

D. Crystalline Structure of Spheroidal Graphite Around the Nucleus

As discussed earlier in this paper, some researchers found disorganized or low crystalline graphite structure around the nucleus. According to Tartera et al.,[14] diamond polishing during metallographic preparation can remove the nuclei from the graphite and leave voids. This creates conditions for stress relaxation in the graphite which is conducive to the herring-bone configuration. Laffont et al.[11] contend that the "disoriented zone" in the core of the graphite obtained from rapidly solidified iron is the product of mechanical deformation occurring when the liquid contracts during its solidification in the metastable system. Subsequent heat treatment leads to the recrystallization of
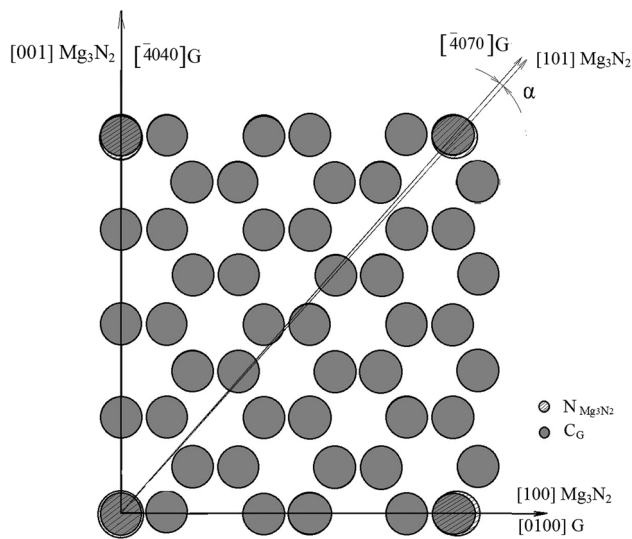

Fig. 9—Correlation between the crystallographic structure of graphite in the plane P_0:{0001} and Mg_3N_2.

Table III. Data for Calculation of Linear Disregistry Graphite-Mg_3N_2

No.	Interatomic Distances for Mg_3N_2[29] (nm)		Interatomic Distances for C-C_{Gr} (nm)		Linear Disregistry δ_l (Percent)
	Atoms	Distance	$[uvw]_G$	$d^G_{[uvw]}$	
1	Mg-Mg	0.272	[1000], [0100], [0010]	0.284	4.41
2	N-N	0.331 to 0.35	[1001], [0101], [0011]	0.3643	0 to 10.06

Table IV. Data for Calculation of Planar Disregistry Graphite-AlN

No.	Planar Disregistry Between	$[uvw]_{AlN}$	$[uvw]_G$	$d^{AlN}_{[uvw]}$	$d^G_{[uvw]}$	α (Deg)	$d^{AlN}_{[hkl]} \cdot \cos\alpha$
1	P_4:($1\bar{2}12$) and AlN	$[10\bar{1}0]$	$[0101]$	0.311	0.3597	0	0.311
2		$[10\bar{1}1]$	$[\bar{2}121]$	0.5871	0.6095	4°11′9″	0.5855
3		$[1001]$	$[\bar{2}020]$	0.498	0.492	0	0.498

the graphite in the core. However, such explanations cannot be extended to graphite in standard spheroidal graphite irons solidifying in the stable system, such as the one discussed by Hara *et al.*[9] While the amorphous center of graphite spheroids found in quenched and then annealed steel could be associated with carbon-rich amorphous regions connected with partially dissolved initial cementite formed from the quenched martensite during early stages of annealing,[10] this argument may cannot be extended to spheroidal graphite in cast iron where nucleation occurs on inclusions.

There is substantial SEM experimental evidence that during stage-I spheroidal graphite grows through a mechanism involving curved-circumferential platelets or foliated growth.[1,3,5,6,32] While there is no consensus on what causes the curvature of graphite during growth, there is strong support to consider the local surface energy as being the root cause (see extensive discussion in Reference 6). The concentric distributions of voids in

the central part of the graphite nodule exposed through high-resolution 3D tomography[33] (Figure 10) further supports the curved-circumferential growth mechanism in the early stages of spheroidal graphite growth. However, oxygen plasma-etched samples (Figure 11) point to a different growth mechanism of the curved crystals than originally proposed by Sadocha and Gruzleski.[5] Indeed, while curved-circumferential growth is clearly observed, continuous spiraling of the graphite plates is not apparent.

We further note that, when the nucleus is spherical, the platelets are less disorganized as compared with the case of cuboidal or prismatic nuclei. Indeed, MgS or (MgCa)S nuclei (Figures 1(a), 2(a), and 1(b)) promote early envelopment of the inclusion by graphite, and with less defects, than for cubic (TiZr)(CN) inclusions (Figure 2(b)), or (MgSiAl)N inclusions (Figure 3), or Mg-La-Ce phosphides.[3] It is thus reasonably to conclude that the nuclei have a significant effect in the early development of the graphite aggregate.
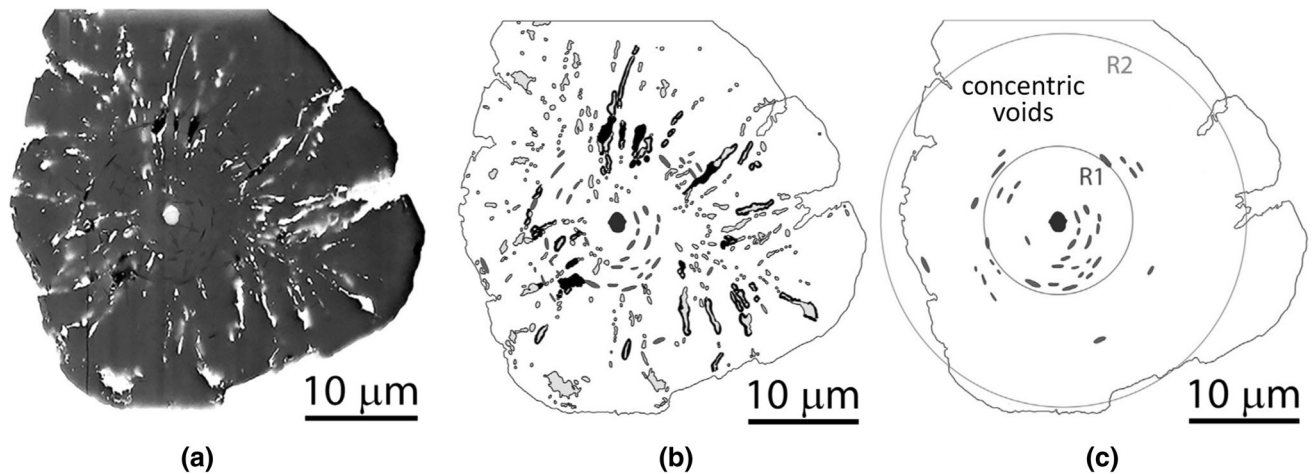

Fig. 10—Concentric voids in the central part of a graphite spheroid: (*a*) 2-dimensional cross section of the graphite nodule at the center of the graphite; (*b*) a binary sketch of (a) showing light-gray Fe particles and micro-voids in black; (*c*) a binary sketch of (a) showing voids perpendicular to the radial direction in the graphite; regions R1 and R2 show distinctively different growth patterns, from Ref. [33] with permission.
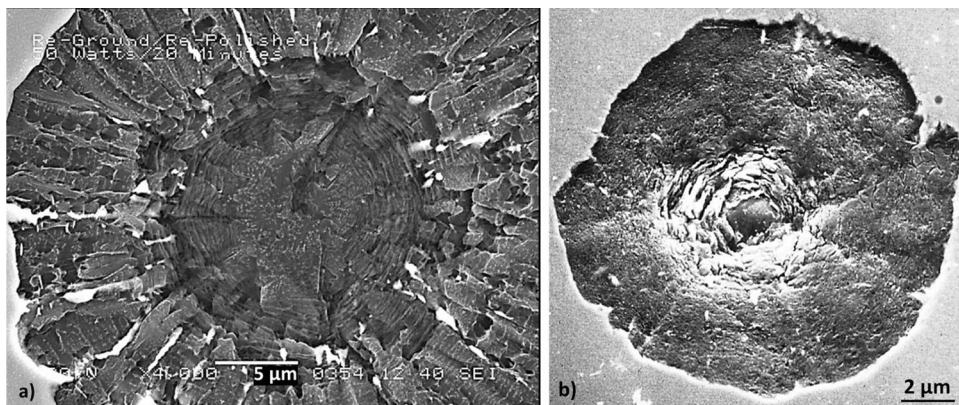

Fig. 11—Oxygen plasma-etched graphite spheroids: (*a*) two regions showing different growth mechanisms, curved-circumferential in the center and conical sectors made of polyhedral blocks on the outside; (*b*) curved-circumferential growth around the MgS nucleus (compliments of Comanches Technologies).

We suggested earlier[6] that such early graphite structure has a low degree of crystallization, consistent with the observation of relatively low crystallinity when observed by TEM. Adsorption of C atoms on the surface of the nucleant at the beginning of the process is a local event. The graphite/nucleant contact does not occur on large surfaces. This is common for the nucleation of lamellar graphite, but, as shown for the first time, it is also the case for spheroidal graphite (see Figure 3). For spheroidal graphite, more than for lamellar graphite, multiple nucleation events occur on the surface of one nucleant. Their growth generates the final shape of the graphite aggregate. Recrystallization during subsequent cooling, or growth of thick graphite plates, may then explain the highly ordered core of spheroids found by other researchers.

IV. CONCLUSIONS

Titanium carbonitrides and complex Mg-Si-Al nitrides are shown to be nucleants for spheroidal graphite in iron-carbon-silicon alloys. Thermodynamic analysis and disregistry calculations for Mg_3N_2 and AlN support the assertion that these nitrides are possible nucleants for graphite. Thus, a complex nitride such as Mg-Si-Al nitride would be a good nucleant for graphite, especially so if it is an associative compound that is an association of stoichiometric compounds. For the first time we bring direct evidence of the disorientation of graphite platelets growing around the graphite nuclei for the particular case of Mg-Al-Si nitrides. This is consistent with the "small crystals randomly twisted" observed by Laffont et al.[11] or with the mixture of distorted and ordered graphite regions observed by Hara et al.[9] It is thus concluded that the low crystallinity of the core of some of the graphite spheroids found in magnesium-modified iron-carbon-silicon alloys is the result of random orientation of the graphite platelets growing on inclusions during early solidification and of subsequent curved-circumferential growth. Understanding the mechanism of nucleation and growth of spheroidal graphite will eventually be conducive to the control and avoidance of degenerated graphite such as exploded or chunky graphite in large castings.

REFERENCES

1. M.J. Lalich and J.R. Hitchings: *AFS Trans.*, 1976, vol. 84, pp. 653–64.
2. J. Tartera, N. Llorca-Isern, M. Marsal, M. Puig, and M. Español: *Int. J. Cast Metals Res.*, 1999, vol. 11, pp. 459–64.
3. D.M. Stefanescu, G. Alonso, P. Larrañaga, E. De la Fuente, and R. Suarez: *Acta Mater.*, 2017, vol. 139, pp. 109–21.
4. J. Qing, V.L. Richards, and D.C. Van Aken: *Carbon*, 2017, vol. 116, pp. 456–69.
5. J.P. Sadocha and J.E. Gruzleski: in *The Metallurgy of Cast Iron*, B. Lux, I. Minkoff, and F. Mollard, eds., Georgi Publishing Co., St Saphorin, 1975, pp. 443–59.
6. D.M. Stefanescu, G. Alonso, P. Larrañaga, E. De la Fuente, and R. Suarez: *Int. J Metalcast.*, 2018, vol. 12 (4), pp. 722–52.
7. K. Yamane, H. Yasuda, A. Sugiyama, T. Nagira, M. Yoshiya, K. Morishita, K. Uesugi, A. Takeuchi, and Y. Suzuki: *Metall. Mater. Trans. A*, 2015, vol. 46A, pp. 4937–46.
8. B. Tonn, J. Lacaze, and S. Duwe: *Mater. Sci. Forum*, 2018, vol. 55, pp. 62–69.
9. T. Hara, T. Kitagawa, K. Kuroki, S. Saikawa, K. Terayama, S. Ikeno, and K. Matsuda: *Mater. Trans. JIMM*, 2014, vol. 55 (9), pp. 1500–05.
10. K. He, H.R. Daniels, A. Brown, R. Brydson, and D.V. Edmonds: *Acta Mater.*, 2007, vol. 55, pp. 2919–27.
11. L. Laffont, R. Jday, and J. Lacaze: *Metall. Mater. Trans. A*, 2018, vol. 49A, pp. 1287–94.
12. J.P. Monchoux, C. Verdu, G. Thollet, R. Fougères, and A. Reynaud: *Acta Mater.*, 2001, vol. 49, pp. 4355–62.
13. K. Theuwissen, J. Lacaze, and L. Laffont: *Carbon*, 2016, vol. 96, pp. 1120–1286.
14. J. Tartera, E. Ochoa de Zabalegui, M. Marsal, and G. Varela-Castro: *Proceedings of The Carl Loper Cast Iron Symposium*, The University of Wisconsin, Madison, May 27–29, 2009.
15. D.D. Li, R.X. Tan, J.X. Gao, B.Q. Wei, Z.Q. Fan, Q.Z. Huang, and K.J. He: *Carbon*, 2017, vol. 111, pp. 428–38.
16. G. Alonso, P. Larrañaga, D.M. Stefanescu, E. De la Fuente, A. Natxiondo, and R. Suarez: *Int. J. Metalcast.*, 2017, vol. 11 (1), pp. 14–26.
17. G. Alonso, D.M. Stefanescu, P. Larrañaga, E. De la Fuente, and R. Suarez: *AFS Trans.*, 2017, vol. 125, pp. 131–46.
18. D.M. Stefanescu, G. Alonso, P. Larrañaga, and R. Suarez: *Acta Mater.*, 2016, vol. 103, pp. 103–14.
19. C.X. Sun and C.R. Loper: *AFS Trans.*, 1983, vol. 91, pp. 639–46.
20. M.H. Jacobs, T.J. Law, D.A. Melford, and M.J. Stowell: *Metals Technol.*, 1974, vol. 11, pp. 490–500.
21. Y. Igarashi and S. Okada: *Int. J. Cast Metals Res.*, 1998, vol. 11 (2), pp. 83–88.
22. J.K. Solberg and M.I. Onsøien: *Mat. Sci. Tech.*, 2001, vol. 17 (10), pp. 1238–42.
23. H. Nakae and Y. Igarashi: *Mater. Trans.*, 2002, vol. 43 (11), pp. 2826–28.
24. G. Alonso, D.M. Stefanescu, E. De la Fuente, P. Larrañaga, and R. Suarez: *Mater. Sci. Forum*, 2018, vol. 925, pp. 78–85.
25. T. Skaland, Ø. Grong, and T. Grong: *Metall. Trans.*, 1993, vol. 24A, pp. 2321–45.
26. B.L. Bramfitt: *Metall. Trans.*, 1970, vol. 1, pp. 1987–95.
27. J.A. Reynolds and C.R. Tottle: *J. Inst. Metals*, 1951, vol. 80, p. 1328.
28. O. Kubachewski and E.L. Evans: *Metallurgical Thermochemistry*, Butterworth-Springer LTD, London, 1951.
29. D.E. Partin, D.J. Williams, and M. O'Keeffe: *J. Solid State Chemistry*, 1997, vol. 132, pp. 56–59.
30. B Lux: in *Recent Research in Cast Iron*, HD Merchant, ed., Gordon and Breach Publsh, New York, 1968, pp. 241–80.
31. E. Ruiz, S. Alvarez, and P. Alemany: *Phys. Rev. B*, 1994, vol. 49 (11), pp. 7115–23.
32. S. Amini and R. Abbaschian: *Carbon*, 2013, vol. 51, pp. 110–23.
33. E. Ghassemali, J.C. Hernando, D.M. Stefanescu, A. Dioszegi, A.E.W. Jarfors, J. Dluhoš, and M. Petrenec: *Scripta Mater.*, 2019, vol. 161, pp. 66–69.